NANO: Brief Reports and Reviews
Vol. 13, No. 7 (2018) 1850074 (14 pages)

DOI: 10.1142/S1793292018500741

Electric, Thermoelectric and Magnetic Properties of Nickel(II) Imine Nanocomplexes

A. Elshafaie*, Laila H. Abdel-Rahman†, Ahmed M. Abu-Dief†, Samar Kamel Hamdan†, A. M. Ahmed* and E. M. M. Ibrahim*,‡

*Physics Department, Faculty of Science
Sohag University, Sohag 82524, Egypt

†Chemistry Department, Faculty of Science
Sohag University, Sohag 82524, Egypt
‡e.ibrahim@science.sohag.edu.eg

Received 4 February 2018
Accepted 22 May 2018
Published 18 July 2018

Production of novel organic semiconductor nanomaterials is essential for enabling the development of personal, portable and flexible electronic modules. This work presents Ni(II)-Schiff base complexes with enhanced Seebeck coefficient and weak ferromagnetic ordering for thermoelectric and magnetic devices. Four Ni(II)-Schiff base complexes (namely $[Ni(C_{12}H_{10}N_3O_4Br)]\cdot 2H_2O$, $[Ni(C_{16}H_{11}N_3O_4)]\cdot 2H_2O$, $[Ni(C_{21}H_{14}N_5O_8Br)]$ and $[Ni(C_{25}H_{17}N_5O_8)]\cdot 1/2H_2O$) have been synthesized in nanosized dimensions. The electrical and thermoelectric properties have been studied, and comprehensive discussions have been presented to understand the electrical conduction mechanisms. The electrical conductivity measurements reveal that the conduction is due to the charge carriers hoping between the atomic sites of the same energy levels in the molecule as well as the transfer of the charge carriers between the neighboring complex molecules due to overlapping of their orbitals. The thermoelectric measurement confirms that the nanocomplexes (NCs) are non-degenerate P-type semiconductors with enhanced Seebeck coefficient values compared with those reported for other organic materials. The NCs exhibit antiferromagnetic to paramagnetic transitions with the increase of temperature and weak ferromagnetic ordering at 300 K.

Keywords: Ni-Schiff base complexes; electric, thermoelectric; magnetic; nanostructures.

1. Introduction

Recent interest in the development of nanodevices for various applications has generated a huge thrust on producing semiconductor nanostructures of adequate compositions and properties. Synthesis and characterization of bulk transition metal complexes with imines as ligands have received overwhelming attention in recent times due to many advantages such as low cost, light weight, mechanical flexibility and low temperature solution process ability. These complexes are promising candidates for many catalytic, magnetic and biological applications beside the development of personal, portable and flexible thermal modules.[1–6] Nevertheless, few works were reported on studying the physical properties of metal–imine complexes,[7] particularly those of nanometric dimensions. Besides, most of the few published studies do not take into account the convenient approach for describing the conduction mechanisms, the majority

‡Corresponding author.

carriers (holes or electrons) which govern the electrical conduction and the magnetic phases in the complexes. Sarkar *et al.*[8] studied the electrical properties of bulk oxovanadium (IV) complexes. They found that the complexes are electrical insulator at room temperature but their electrical conductivity increases as the temperature increases from 330 K, indicating an *n*-type semiconducting behavior with activation energies from 0.48 eV to 1.18 eV. The results suggested the feasibility of using these complexes in many electronic applications.

The magnetic properties of 3d metal complexes, in general, have been studied to investigate the influence of various parameters such as size, crystal lattice defects and surface effects.[9] It was reported that variation of these parameters leads to novel and interesting magnetic properties.[10–12] In particular, Ni complexes have aroused wide public concern for using as magnetic catalysis.[13,14] In this context, many Ni complexes were synthesized in other previous works. For example, Xiao *et al.*[15] synthesized heptanuclear cluster $[Ni_7(immep)_6(MeO)_6]\cdot(NO_3)_2$ using microwave-assisted reaction of $Ni(NO_3)_{2\cdot6}H_2O$ with 2-hydroxy-3-ethoxy-benzaldehyde and ammonium water in mixed solvent (acetonitrile:methanol = 1:1). The synthesized complex shows antiferromagnetic to paramagnetic transition at 25 K. Furthermore, the Weiss constant has a large positive value, indicating an intramolecular ferromagnetic interaction between adjacent Ni^{II} ions.

In the present work, we give some insights into the electrical, thermoelectric and magnetic properties of $[Ni(C_{12}H_{10}N_3O_4Br)]\cdot2H_2O$, $[Ni(C_{16}H_{11}N_3O_4)]\cdot2H_2O$, $[Ni(C_{21}H_{14}N_5O_8Br)]$ and $[Ni(C_{25}H_{17}N_5O_8)]\cdot1/2H_2O$ (denoted as NiL_1, NiL_2, NiL_3 and NiL_4, respectively) nanocomplexes (NCs). Comprehensive discussions have been presented in order to understand the electrical conduction mechanisms. DC and AC magnetic measurements have been employed to understand the magnetic features of the complexes.

2. Experimental Work

2.1. *Synthesis of imine ligands*

2.1.1. *Synthesis of L_1 and L_2 imine ligands*

The tridentate imine ligands (L_1 and L_2) were synthesized by the condensation of equimolar ratio of 5-bromosalicyaldehyde (5 mmol, 1.00 g) or 2-hydroxy-1-napthaldehyde (5 mmol, 0.86 g) with 2-aminopyridine (5 mmol, 0.47 g) in ethanol. The resulting reaction mixtures were refluxed for 1 h at 70°C. After that, solutions were gradually evaporated to quarter of its original volume and then left to cool. The obtained orange and yellow crystals of imine ligands were filtered and then washed with cold ethanol several times and dried under reduced pressure in a desiccator. Note that the purity of the compounds was tested by TLC silica gel.[16]

2.1.2. *Synthesis of L_3 and L_4 imine ligands*

4-nitro-o-phenylenediamine (5 mmol, 0.77 g) in 25 mL of ethanol was slowly added to ethanolic solution (25 mL) containing isatin (5 mmol, 0.74 g), followed by the slow addition of 5-bromosalicylaldehyde (5 mmol, 1.00 g) or 2-hydroxy-1-napthaldehyde (5 mmol, 0.86 g) dissolved in 25 mL ethanol. A colored precipitate was obtained on refluxing the solution for 3 h.[16] The precipitate was filtered by suction and washed thoroughly with ethanol. The pure compounds were dried in desiccator over anhydrous calcium chloride. The purity of the product was checked by TLC.[16,17]

2.2. *Synthesis of Ni(II) imine NCs*

2.2.1. *Synthesis of $[Ni(C_{12}H_{10}N_3O_4Br)]\cdot2H_2O$ (NiL_1) and $[Ni(C_{16}H_{11}N_3O_4)]\cdot2H_2O$ (NiL_2) NCs*

An aqueous ethanolic solution of $Ni(NO_3)_2\cdot6H_2O$ (5 mmol, 8 mL) was added dropwise to the solution of prepared imine ligand (5 mmol, 15 mL) and the mixture was stirred for 3 h[18,19] (see Scheme 1). Then the obtained solid precipitate was filtered, washed with ethanol and then dried in vacuo over anhydrous $CaCl_2$.

2.2.2. *Synthesis of $Ni(C_{21}H_{14}N_5O_8Br)]$ (NiL_3) and $[Ni(C_{25}H_{17}N_5O_8)]\cdot1/2H_2O$ (NiL_4) NCs*

The NiL_3 and NiL_4 NCs were synthesized by the addition of 5 mmol of $Ni(NO_3)_2\cdot6H_2O$ (1.45 g); (1.00 g) dissolved in about 30 mL of ethanolic solution into a hot ethanolic solution 30 mL (5 mmol, 2.32 g) of each imine ligand (HL_3, HL_4) in molar ratio (1:1). It was observed that the color of the NCs changed immediately. The resulting mixture was refluxed with stirring for 1 h. After evaporation of the solvent, the precipitated solid was filtered off from the reaction mixture, thoroughly washed with ethanol and desiccated over anhydrous calcium chloride (see Scheme 2).

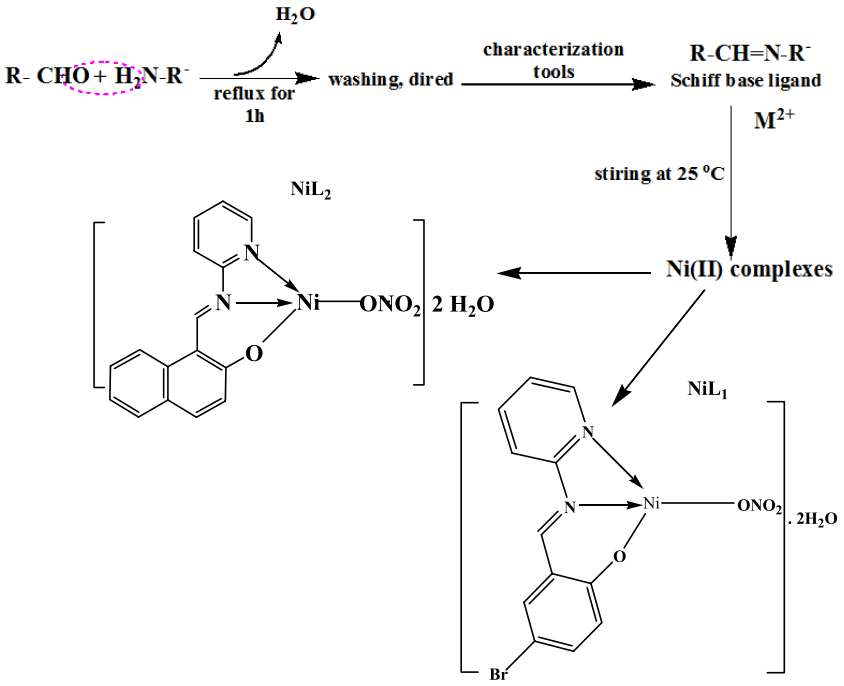

Scheme 1. Digrammatic scheme for the synthesis of tridentate imine ligands and their NiL_1, NiL_2 complexes.

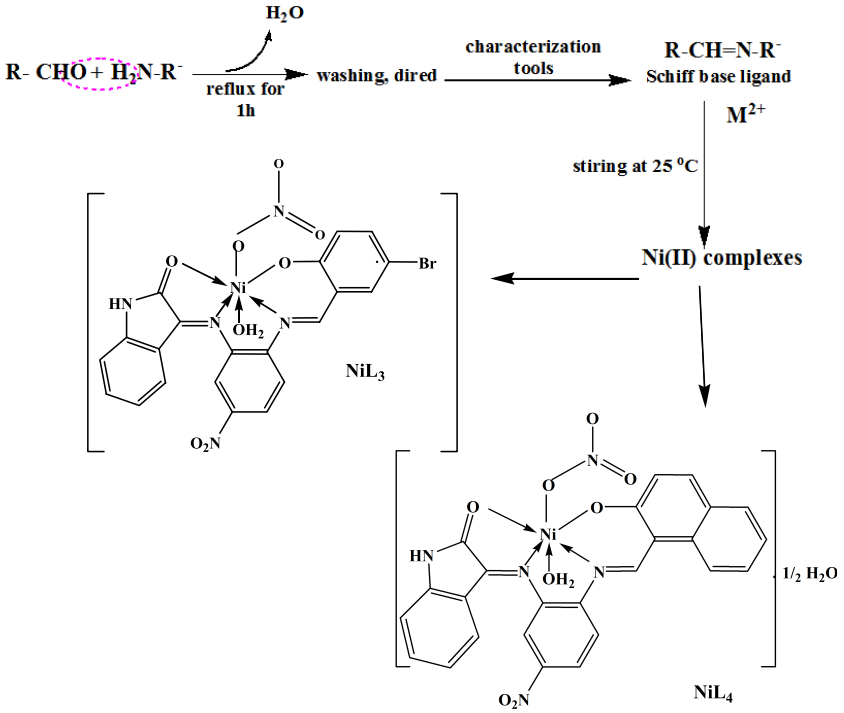

Scheme 2. Digrammatic scheme for synthesis of tetradentate imine ligands and their Ni(II) complexes.

2.3. *Measurement and characterization systems*

NMR spectra of the ligands were measured on multinuclear FT-NMR spectrometer Bruker AR × 400 at 400.1 MHz (1H) and 100.6 (13C) MHz using deuterated N, N'-dimethylsulfoxide (DMSO-d6). A Perkin-Elmer 240c Elemental analyzer was used to micro-analytical data (C, H and N). Magnetic

measurements of complexes were determined on Gouy's balance; the diamagnetic correction was made by Pascal's contents and Hg[Co(SCN)4] as a calibrant. The FT-IR spectra of the compounds were recorded on Shimadzu FTIR 8101 spectrophotometer using KBr discs. Electronic spectra for the prepared ligands and their complexes were recorded on Jasco P-530 UV-visible spectrophotometer model T + 80 using 10 mm matched quartz cells, and data were reported in λmax/nm. TGA analyses were recorded on a Shimaduz cooperation 60 H analyzer under a dynamic flow of nitrogen atmosphere (40 mL/min) and heating rate 10°C/min from ambient temperature to 750°C.

Transmission electron microscopy (TEM) investigation was carried out using a TEM — 2100, with Schottky field emission gun at 300 kV. The DC magnetic properties were determined with a vibrating sample magnetometer VSM model LDJ 9600 in an applied magnetic field up to 1 T. The AC magnetic properties were studied by means of Bartington Instrument MS2C system in the temperature range 90–405 K and external applied magnetic field 250 μT, where the equipment was located in a place away from the potential sources to avoid the electrical noise, and the powder samples were fixed in ceramic cylindrical pillboxes.

The electrical properties were studied by measuring the temperature dependence of the electrical conductivity using the two-prop method in the temperature range 370–595 K. The temperature dependence of Seebeck coefficient was determined in order to study the thermoelectric properties of the synthesized materials. The measurements were carried out within a temperature range 83–313 K using specially made sample holder. The electrical conductivity and Seebeck coefficient measurements were carried out in a vacuum of 10^{-3} mmHg, which was found to contribute much to the thermal stability during the measurements.

3. Results and Discussion

3.1. *Physicochemical properties of the prepared imine ligands and their complexes*

3.1.1. *^{1}H NMR and ^{13}C spectral studies of the prepared imine ligands*

The prepared imine ligands were characterized by the ^{1}H NMR (400 MHz and δ/ppm) in DMSO-d_6.

Table 1. ^{1}H NMR spectroscopic data of the tri and tetradentate imine ligands in DMSO.

Imine ligands	^{1}H NMR (δ, ppm) in DMSO-d_6
L_1	12.80 (s, 1H, OH), 9.50 (s, 1H, =CH), 8.50 (d, 1H, CH pyridine), 6.90–8.00 (m, 6H, ArH)
L_2	15.19 (s, 1H, OH), 9.85 (s, 1H, =CH), 8.26 (d, 1H, m-py), 7.95 (d, 1H, p-py), 7.90 (d, 1H, m-py), 7.74 (d, 1H, ArH napthyl), 7.63 (d, 1H, ArH napthyl), 7.54 (t, 1H, ArH napthyl), 7.36–7.30 (m, 2H, ArH napthyl), 6.86 (m, 2H, ArH napthyl)
L_3	11.61 (s, 1H, OH), 8.94 (s, 1H, =CH), 7.56 (s, 1H, NH), 8.11 (s, 1H, H-C6, *o*-NO_2), 7.95 (d, 2H, ArH), 7.62–6.65 (d, 3H, ArH, 5-bromosalicyaldehyde) 7.91 (s, 1H, H-C7, isatin), 6.81–6.77 (t, 3H, H-C6, isatin)
L_4	14.58 (s, 1H, OH), 10.82 (s, 1H, CH=N), 9.76 (s, 1H, H-C6, *o*-NO_2), 8.64–8.19 (d, 2H, ArH), 8.94–7.99 (d, 4H, naphthyl), 6.67 (s, 2H, naphthyl), 7.91 (d, 1H, H-C7, isatin), 7.60–7.23 (t, 3H, H-C6, isatin), 7.25 (s, 1H, NH)

The characteristic data of ^{1}HNMR for the ligands are depicted in Table 1.

The ^{1}H NMR spectrum of imine ligand (L_1) showed two singlet signals at $\delta = 12.80$ ppm and 9.50 ppm, which are assigned to the phenolic −OH and characteristic azomethine (CH=N) protons of the ligand, respectively. Also, it shows doublet signals at 8.50 ppm and 8.20 ppm for aromatic protons of CH of pyridine ring. Furthermore, signals of phenyl ring protons appeared as multiplets in the range of 6.90–8.00 ppm. The ^{1}H NMR spectrum of the prepared imine ligand (L_2) (cf. Fig. 1) showed singlet signal due to −OH proton at 15.19 ppm.[20] The higher values of δ for the −OH group can be assigned to the presence of intermolecular hydrogen bonding.[21] The OH signal disappears with the addition of D_2O. The characteristic proton of azomethine appeared as singlet at 9.85 ppm. Moreover, the signals of CH pyridine ring are found as doublet in the range between 8.26 ppm and 7.90 ppm.

In contrast, aromatic protons of naphthyl ring were found as multiplets in the range of 7.74–6.86 ppm. The ^{1}H NMR spectrum of imine ligand (L_3) exhibited singlet signal at 11.61 ppm for (−OH) group. The signal due to the azomethine proton (−HC=N) is observed at $\delta = 8.94$ ppm.[22] The signals due to aromatic protons of 5-bromosalicyaldehyde

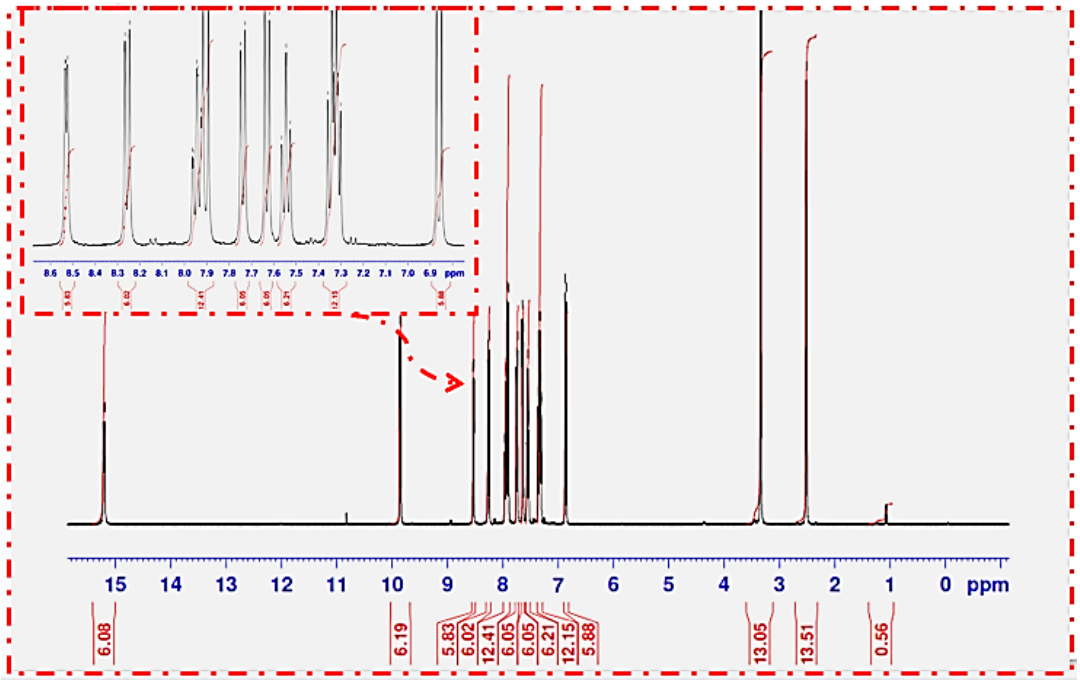

Fig. 1. ^{1}H NMR spectrum of L_2 imine ligand.

and 4-nitro-o-phenylenediamine have resonated as doublet in the region of 8.11–6.65 ppm. The proton of the amide "NH" group appeared as singlet at 7.56 ppm. The signals are due to isatin protons as doublet at 7.91 ppm and triplet in the region 6.81–6.77 ppm. In the ^{1}HNMR spectrum of imine ligand (L_4) displayed singlet signal at 14.58 ppm due to the proton of OH group. The signal due to azomethine proton resonated at 10.82 ppm. The signals due to aromatic protons of napthyl and 4-nitro-o-phenylenediamine have resonated as multiplets in the region of 9.76–7.99 ppm. The proton of the amide "NH" group appeared as singlet at 7.25 ppm. The signals due to isatin protons appear as doublet at 7.91 ppm and triplet in the region 7.43–6.67 ppm. It was noticed that DMSO did not have any coordinating effect on the prepared ligands.

^{13}C NMR spectral data were consistent with ^{1}H NMR spectral data. The characteristic signals of ^{13}CNMR for the ligands are depicted in Table 1.

^{13}C NMR of L_1 imine ligand exhibited signal at 163.1 ppm, which may be assigned to azomethine carbon. The signals observed in the region 112.3–190 ppm were assigned to phenyl carbon. The ^{13}C NMR spectrum of L_2 imine ligand (cf. Fig. 2) showed signal at 176.9 ppm due to the characteristic azomethine carbon. The ligand also exhibited signals at 108.6 (C_q, C-CH=N), 115.8 (CH), 120.1 (CH), 122.0 (CH), 124.3 (CH), 124.4 (CH), 127.0 (C_q, napthyl), 129.1 (CH), 129.6 (CH), 134.1 (C_q, −OH), 139.3 (CH *m*-py), 139.5 (CH *m*-py), 149.4 (CH *p*-py), 151.5 (CH, *o*-py) and 153.6 (C_q-py). ^{13}C NMR spectra of L_3 ligand exhibited sharp signals at 112.7, 119.4, 123.1, 124.7, 150.6 and 158.9 ppm due to isatin moiety. In contrast, the signals associated with aromatic carbons of 5-bromosalicyaldehyde and 4-nitro-o-phenylenediamine appeared at 110.8, 114.6, 113.7, 133.2, 134.1, 135.9 and 138.8 ppm. Whereas the characteristic signals associated with imine carbons and carbonyl group of L_3 ligand were found at 176.0 ppm, 208.2 ppm and 250.00 ppm, respectively. ^{13}C NMR spectra of L_4 ligand exhibited sharp signals at 113.9, 116.2, 127.9, 124.7, 149.8 and 124.1 ppm due to isatin moiety. On the contrary, the signals associated with aromatic carbons of 2-hydroxy-1-napthaldehyde and 4-nitro-o-phenylenediamine appeared at 110.5, 120.0, 121.6, 128.5, 129.3, 133.1, 137.3, 163.7 and 167.2 ppm. Whereas the characteristic signals associated with imine carbons and carbonyl group of L_4 ligand were found at 168.0 ppm, 181.8 ppm and 234.7 ppm, respectively.

3.1.2. *Infrared spectra for the prepared imine ligands and their NCs*

Infrared spectra of the imine ligands and their Ni(II) NCs were recorded in KBr pellets from 4000 cm^{-1}

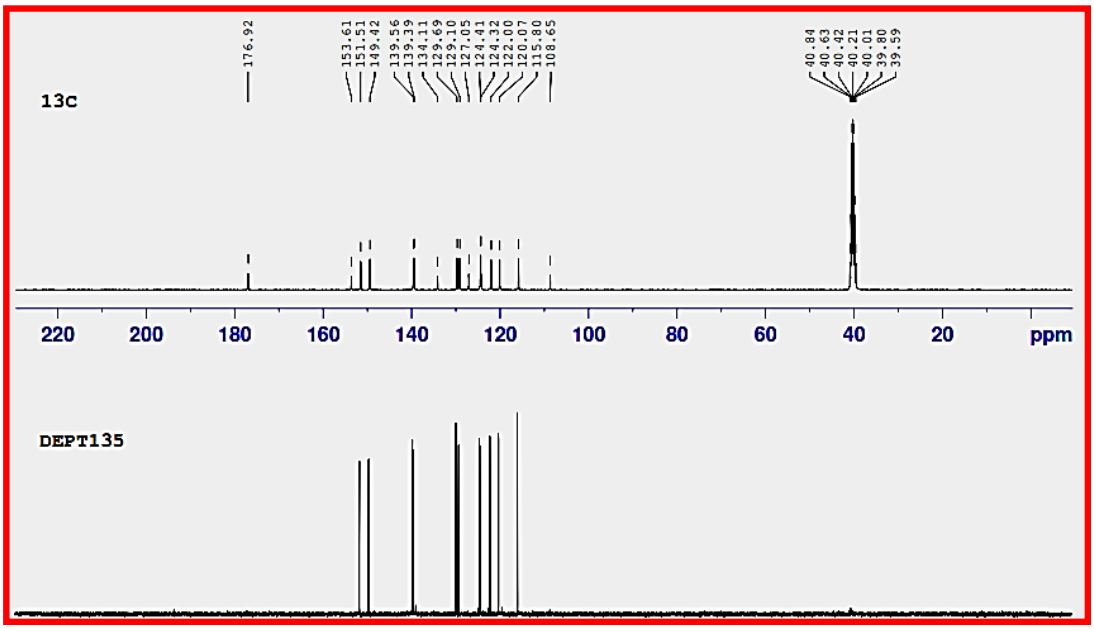

Fig. 2. ^{13}C NMR spectrum of L_2 imine ligand.

to 400 cm^{-1}. The induced bands give fundamental information about the nature of the functional group attached to the metal atom. The IR spectra of Schiff ligands and their complexes are found to be quiet complicated because it exhibits large number of bands of varying intensities. The results of the IR spectra are summarized in Table 2, and Fig. 3 shows the IR spectrum of imine ligand L_2 and its corresponding Ni-Schiff base NCs (NiL_2) as examples. The spectra of imine ligands L_1 and L_2 exhibit characteristic bands at 3333–3426 cm^{-1} due to the stretching vibration of the OH group.[23] These bands disappeared in the NCs and substituted, in the same place, by other bands within 3434–3467 cm^{-1} assigned to the stretching motion of the uncoordinated water molecules.[24] The phenolic (C–O) stretching vibrations appeared at 1325 cm^{-1} and 1312 cm^{-1} in L_1 and L_2 ligands, respectively, shifted toward lower frequencies (1289–1310 cm^{-1} and 1250–1304 cm^{-1}) in the NCs. The shift of these bands to lower wave number values upon complexation confirms the involvement of oxygen atom of phenolic group in the chelation with C–O–M.[25] The spectra of the HL_1 and HL_2 ligands show strong bands at 1645 cm^{-1} and 1630 cm^{-1} due to an azomethine group (C=N) stretching vibration which indicates the presence of the imine structure.[26–28]

Table 2. The infrared absorption wave numbers (cm^{-1}) of the prepared imine ligands and their Ni(II) NCs.

Compounds	(υOH)/H_2O	(υNH)	(υCH)$_{ar}$	υ(C=N)	υ(C=N)$_{py}$	(υC=O)	υ(C–O)$_{ph}$	(υM–O)	(υM–N)
L_1	3333 (b)	—	3051(w)	1645 (vs)	1590 (s)	—	1325 (m)	—	—
NiL_1	3468 (w)	—	3020 (w)	1600 (vs)	1578 (s)	—	1310 (m)	566 (w)	450 (w)
L_2	3426 (s)	—	3030 (w)	1630 (vs)	1585 (s)	—	1315 (m)	—	—
NiL_2	3450 (w)	—	3064 (w)	1615 (vs)	1570 (s)	—	1304 (m)	518 (w)	453 (w)
L_3	3464 (b)	3196 (w)	3068 (w)	1627 (vs) 1607 (s)	—	1736	1308 (m)	—	—
NiL_3	—	3200 (w)	3060 (w)	1606 (vs) 1577 (s)	—	1690	1271 (m)	567 (w)	455 (w)
L_4	3437 (b)	3199 (w)	3021 (w)	1634 (vs) 1599 (s)	—	1740	1212 (m)	—	—
NiL_4	3468 (w)	3056 (w)	3039 (w)	1618 (vs) 1569 (s)	—	1699	1167 (m)	668 (w)	475 (w)

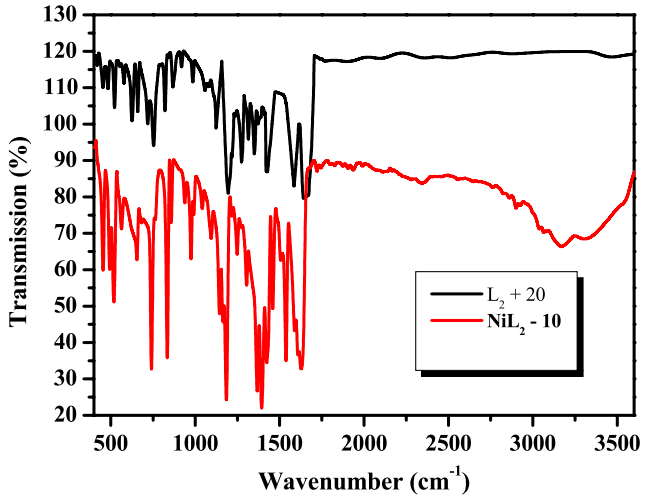

Fig. 3. IR spectra of imine ligand (L_2) and its NiL_2 complex.

These bands shifted to lower wave numbers in the spectra of all the NCs (1600 cm^{-1} and 1615 cm^{-1}), indicating the involvement of the nitrogen atom of the azomethine or imine group in the coordination to the metal ion.[26–28] A strong band appeared at 1590 cm^{-1} and 1585 cm^{-1} for the free HL_1 and HL_2 ligands, respectively, assigned to stretching vibration of pyridyl nitrogen υ(C=N).[24] On complexation, these bands shifted to 1568–1578 cm^{-1} and 1563–1577 cm^{-1}, indicating coordination through pyridine nitrogen.[29] Furthermore, from the spectroscopic behavior of simple metallic complexes of pyridine, it is known that after complexation the vibrations in the high frequency region are not considerably shifted, whereas the ring deformation found at 604 cm^{-1} and 405 cm^{-1} in the free pyridine is shifted to higher frequencies.[30] In the present study, the in-plane ring deformation bands are found at 625–654 cm^{-1} in the HL_1 and HL_2 ligands.[31] These bands are shifted to higher 25–45 cm^{-1} wavenumber showing coordination via pyridine nitrogen.[32] The complexation of metal ions with ligands was further confirmed by the appearance of new weak intensity with non-ligand bands in the region 507–615 cm^{-1} and 450–483 cm^{-1} in the spectra of the NCs, which are assigned to frequencies of υ(M–O) and υ(M–N) stretching vibrations, respectively.[33] In the IR spectra of imine ligands HL_3 and HL_4, absorption of phenolic OH and amide NH has displayed bands at 3464–3437 cm^{-1} and 3196–3199 cm^{-1}, respectively.[34] A high intensity band was observed at 1736–1740 cm^{-1} due to the carbonyl function υ(C=O).[34] Absorption bands due to azomethine function υ(C=N) of HL_3 and HL_4 ligands appear at 1607–1627 cm^{-1} and 1599–1634 cm^{-1}, respectively.[35] Absorption bands due to phenolic (C–O) function of free imine ligands appear at 1212–1308 cm^{-1}.

In the IR spectra of NiL_3 and NiL_4 complexes, it was observed that the absence of absorption bands due to phenolic OH at 3464–3437 cm^{-1} of ligand indicates the formation of bond between metal ion and phenolic oxygen atom *via* deprotontation.[36] This is further confirmed by the decrease in the absorption frequency of phenolic bands υ(C–O) which appeared at the region 1167–1271 cm^{-1} in all metal complexes indicating the participation of the oxygen atom of phenolic group in coordination to metal ions.[37]

In the IR spectra of the metal complexes, medium intensity weak bands appear at 3196–3199 cm^{-1} due to υ(NH). These bands appear almost at the same position as in the case of ligands, thus confirming their non-involvement in coordination with the metal ions.[38] The shift of amide carbonyl υ(C=O) to lower frequencies (1690–1699) cm^{-1} in all the NCs confirms the coordination of oxygen atom of amide υ(C=O) with the metal ions.[34] The absorption frequency of azomethine υ(C=N) function shifted to lower frequency to appear in the region at 1600–1634 cm^{-1} and 1573–1577 cm^{-1}, suggesting the involvement of nitrogen atom of azomethine function in complexation with the metal ions.[26–28] Furthermore, the appearance of broad band at 3447–3468 cm^{-1} in the metal complexes is assigned to υ(OH) of lattice water molecules. The complexation of metal ions with ligand was further confirmed by the appearance of new weak intensity non-ligand bands in the region at 567–668 cm^{-1} and 455–581 cm^{-1} in the spectra of Ni(II) complexes, which are assigned to frequencies of υ(M–O) and υ(M–N) stretching vibrations, respectively.[24] The bands at 1425–1410 cm^{-1} (υ_{asy}), 1311–1325 cm^{-1} (υ_{sy}) and 810 cm^{-1} (υ_{sy}) in the spectra of nickel NCs are due to coordinated nitrate group that are coordinated to the central metal ion in a unidentate fashion. The other bands observed in the region 3060–3080 cm^{-1} can be assigned to υ(CH) aromatic. Furthermore, the peaks found at 822–952 cm^{-1} are assigned to the rocking mode of the coordinated water in the metal complexes.[24]

3.1.3. *Elemental analyses for the prepared compounds*

The results of elemental analyses (C, H, N) of the prepared *Schiff base* ligands and their complexes

Table 3. Analytical and physical data of the prepared imine ligands and their nickel (II) complexes.

Compounds	Empirical formula (Formulae weight)[a]	(M. p.) and decomp. temp. (°C)	μ_{eff} (B.M.)	Analysis (%) Found (Calc.) C	H	N
L_1	$C_{12}H_9N_2OBr$ (276.90)	(140)	—	51.95 (52.01)	3.20 (3.25)	10.06 (10.12)
NiL_1	$[Ni(C_{12}H_{10}N_3O_4Br)]\cdot 2H_2O$ (432.59)	>300	2.72	33.25 (33.29)	2.72 (2.78)	9.68 (9.71)
L_2	$C_{16}H_{12}N_2O$ (248.00)	(170)	—	77.35 (77.42)	4.79 (4.84)	11.25 (11.29)
NiL_2	$[Ni(C_{16}H_{11}N_3O_4)]\cdot 2H_2O$ (403.69)	>300	2.79	47.56 (47.57)	3.63 (3.72)	10.34 (10.40)
L_3	$C_{21}H_{13}N_4O_4Br$ (464.90)	(218)	—	54.15 (54.21)	2.74 (2.80)	11.99 (12.05)
NiL_3	$[Ni(C_{21}H_{14}N_5O_8Br)]$ (602.59)	>300	3.30	41.76 (41.82)	2.26 (2.33)	11.55 (11.62)
L_4	$C_{25}H_{16}N_4O_4$ (436.00)	(228)	—	68.69 (68.81)	3.55 (3.67)	12.73 (12.84)
NiL_4	$[Ni(C_{25}H_{17}N_5O_8)]\cdot 1/2H_2O$ (582.69)	>300	3.30	51.35 (51.49)	2.77 (2.92)	11.93 (12.02)

Note: [a]Formulae weight = g/mol.

are tabulated in Table 3. The chemical formula of the four NCs NiL_1, NiL_2, NiL_3 and NiL_4 are $[Ni(C_{12}H_{10}N_3O_4Br)]\cdot 2H_2O$, $[Ni(C_{16}H_{11}N_3O_4)]\cdot 2H_2O$, $[Ni(C_{21}H_{14}N_5O_8Br)]$ and $[Ni(C_{25}H_{17}N_5O_8)]\cdot 1/2H_2O$, respectively. The melting points and C: H: N ratios were also determined and tabulated in Table 3. The results confirm that the complexes are stable in air and their decomposition temperatures are higher than the reported melting points of their Schiff ligands. This is an evidence for the complexation of the ligands with the Ni ions.[24]

3.1.4. *Molecular electronic spectra of the prepared Schiff base ligands and nickel complexes*

Electronic spectroscopy is an important and valuable tool to draw important information about the structural aspects of the complexes. The ligands, which are mainly organic compounds, have absorption in the ultraviolet region (200–350 nm) of the electromagnetic spectrum and in some cases these bands extend over to higher wavelength region due to conjugation. But upon complexation with transition metal ions, there will be an interesting change in the electronic properties of the system. New features or bands in the visible region due to *d–d* absorption[39] and charge transfer spectra from metal to ligand can be observed, and these data can be processed to obtain information regarding the structure and geometry of the compounds. The electronic spectral data of our imine ligands exhibited peaks around 386–460 nm. The spectral peaks around 386 nm correspond to $n \rightarrow \pi^*$ transitions of azomethine group, whereas the spectral band around 460 nm is assigned to transitions of donating atoms like oxygen and nitrogen which are overlapped with the intermolecular form aromatic rings. Another band appeared below 386 nm can be assigned to $\pi \rightarrow \pi^*$ transitions. On complexation, this band disappeared suggesting the coordination of azomethine nitrogen to the metal ion, as the formation of the metal–nitrogen bond stabilizes the electron pair on the nitrogen atom.[40] Thus, addition of metal ion to the ligand solution causes characteristic changes in the visible absorption spectra of the ligand, suggesting an immediate complex formation in solution. As shown in Fig. 4, the designed complexes display a characteristic band centered at $\lambda_{max} = 310$–393 nm. This band could be mainly ascribed to an intermolecular charge transfer transition taking place in the complexed ligand. Moreover, there is a band shown in the region 454–482 nm, which can be attributed to charge transfer from ligand to metal. Furthermore, the L → MCT band is followed by a broad band from 640 nm to 741 nm. This band could be mainly attributed to $d \rightarrow d$ transition in the prepared complexes.

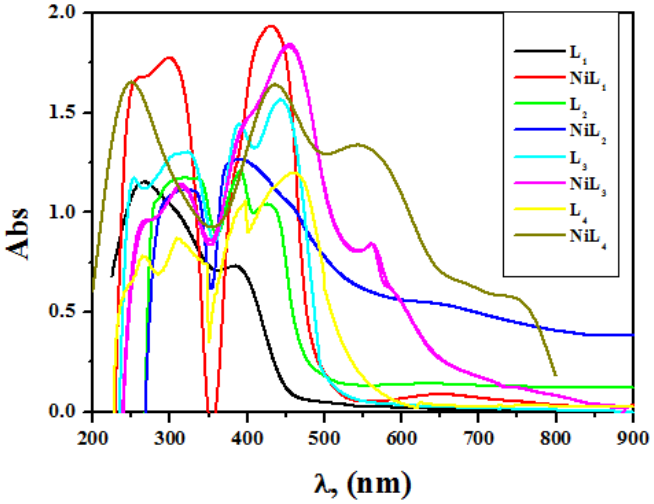

Fig. 4. Molecular electronic spectra of the prepared Schiff base ligands and their Ni(II) NCs.

3.1.5. *Thermogravimetric analysis (TGA) of the prepared Schiff base Ni(II) complexes*

Thermal analysis (TGA) of the metal chelates is an important tool to (i) get information about the thermal stability of these complexes, (ii) decide whether the water molecules (if present) are inside or outside the inner coordination sphere of the central metal ion[41] and (iii) suggest a general scheme for thermal decomposition of these chelates. Heating rates of four samples were suitably controlled at 10°C/min under nitrogen atmosphere, and the weight loss was measured from the ambient temperature up to ∼750°C. The phenomenological aspects of weight loss for each chelate within the corresponding temperature ranges were calculated and provided in Table 4. TGA spectra of the prepared imine complexes show three stages: (i) a small weight loss which is assigned to loss of lattice water molecule, (ii) maximum weight loss which is attributable to the loss of coordinated water molecules and (iii) gradual weight loss which can be assigned to complete decomposition of ligand moiety around the metal ion. After these stages, complexes are converted into nickel ions.[42]

3.2. *Morphology investigation of Ni(II) NCs*

The morphology of the Ni(II) NCs was studied by TEM. The images and corresponding histograms depicted in Fig. 5 illustrate that the complexes have various nanostructures with different sizes. To be specific, the images depicted in Figs. 5(a) and 5(d) show that the NiL_1 and NiL_4 NCs consist of semi-spherical NPs with average diameters 45 nm and 9 nm, respectively. On the other side, the NiL_2 and NiL_3 NCs consist of nanowires and nanodendrites with diameters of 250 nm and 115 nm, respectively. These longitudinal shapes of the NiL_2 and NiL_3 nanostructures are due to the closer approach of their tiny NPs which aggregated with each other and then oriented mainly in one direction.

Table 4. Thermal analysis of the prepared Ni(II) complexes.

Complexes	Decomp. temp. (°C)	Weight loss (%) Found	(Calc.)	Decomp. assignment
NiL_1	25–112	8.29	(8.32)	$2H_2O$
	112–250	14.30	(14.33)	NO_3^-
	250–378	21.30	(21.27)	$C_5H_4N_2$
	378–524	42.49	(42.51)	C_7H_4BrO
Residue	> 524	13.62	(13.57)	Ni
NiL_2	16–115	8.89	(8.92)	$2H_2O$
	115–222	7.38	(7.43)	NO
	223–381	30.65	(30.72)	$C_5H_4N_2O_2$
	381–595	38.39	(38.40)	$C_{11}H_7O$
Residue	> 595	14.69	(14.53)	Ni
NiL_3	36–218	2.79	(2.99)	H_2O
	218–376	10.31	(10.29)	NO_3^-
	376–566	55.28	(55.24)	$C_6H_4OBr + C_7H_3N_3O_2$
	566–749	21.78	(21.74)	C_8H_5NO
Residue	> 749	9.84	(9.74)	Ni
NiL_4	39–120	1.60	(1.54)	$1/2H_2O$
	140–222	3.20	(3.09)	H_2O
	222–395	10.82	(10.64)	NO_3^-
	395–478	24.94	(24.88)	$C_8H_5N_2O$
	478–566	29.11	(29.00)	$C_{11}H_7NO$
	566–749	20.05	(20.77)	$C_6H_3NO_2$
Residue	> 749	10.28	(10.08)	Ni

3.3. *Electrical and thermoelectrical properties*

To study the electrical properties of the synthesized samples, the temperature (T) dependence of the electrical conductivity (σ) has been measured in the temperature range 370–595 K. The σ–T plots illustrated in Fig. 6(a) reveal that the Ni(II) NCs show typical thermally activated semiconducting features. This means that by increasing the temperature, more and more charge carriers can overcome the energy barrier and participate in the electrical

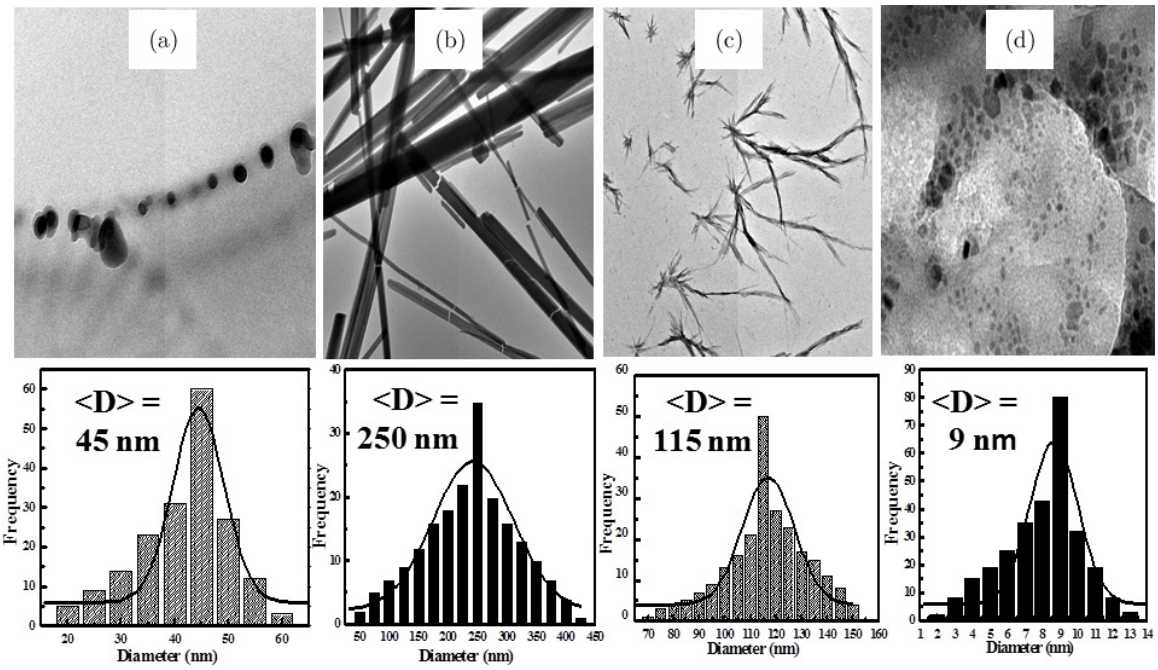

Fig. 5. TEM micrographs and particle size distribution of (a) NiL_1, (b) NiL_2, (c) NiL_3 and (d) NiL_4 nanostructures.

conduction behavior.[43–46] The σ–T plots in Fig. 6(a) are well described by the Arrhenius equation[47]:

$$\sigma = \sigma_o \exp\left(\frac{-E_a}{K_B T}\right), \tag{1}$$

where σ_0 is the pre-exponential factor, E_a is the activation energy for electrical conduction, which is a function of electronic energy levels of the chemically interacting atoms in the materials, and K_B is the Boltzmann's constant. The linear behavior of the Ln σ versus $1000/T$ plots presented in Fig. 6(b) confirms the thermally activated type of conduction.[48] Note that each straight line is divided into two linear portions with different activation energies; herein denoted as E_{inter} and E_{intra} for the low and high temperature ranges of measurement. This behavior indicates a transition between two

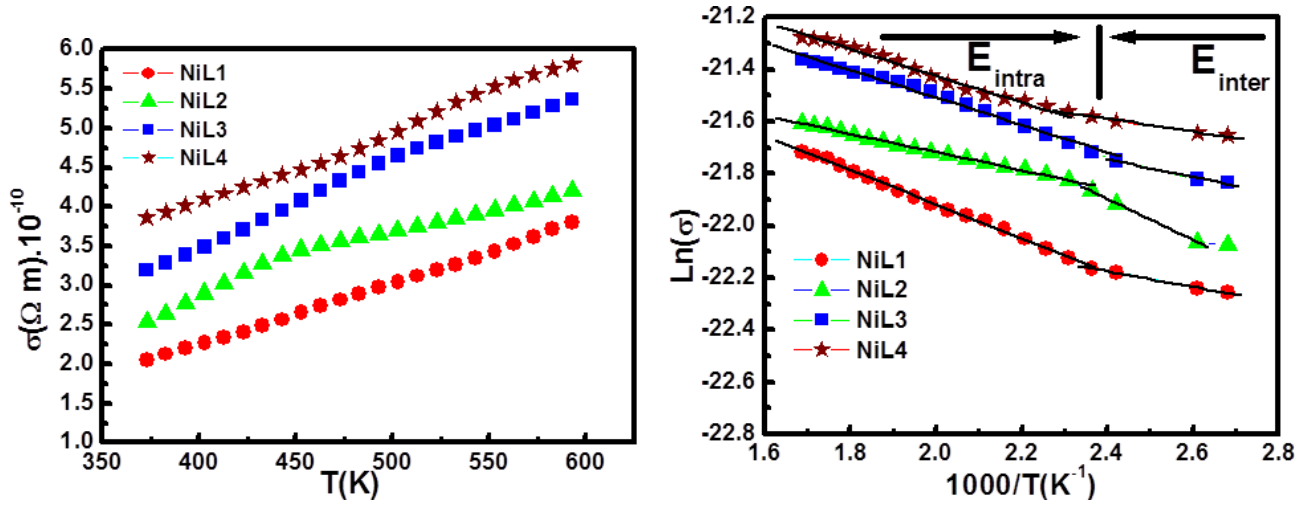

(a) (b)

Fig. 6. (a) The electrical conductivity σ versus temperature (T) of Ni NCs and (b) Ln(σ) versus $1000/T$ of Ni NCs.

Table 5. Activation energies of Ni(II) calculated from electrical conductivity measurement.

Activation energy	NiL_1	NiL_2	NiL_3	NiL_4
E_{inter} (eV)	0.92	0.86	0.73	0.65
E_{intra} (eV)	1.02	1.05	1.08	1.10
E_f (eV)	0.021	0.0164	0.007	0.0025

different conduction mechanisms as the temperature changes. By taking into consideration the microstructure of the complexes, the carrier transfer in the sample can be classified into intramolecular and intermolecular transfer types. In the intramolecular transfer, the electron moves in the molecule where it hops from one atomic site to another if orbitals exist at these sites with the same energy levels, i.e., the intramolecular conduction mechanism occurs between the metal atom and the ligand in the complex molecule, whereas the intermolecular mechanism occurs due to the carriers transfer between the neighboring complex molecules due to overlapping of their orbitals.[49] Accordingly, the corresponding activation energy E_{inter} (characterizing the low temperature range of measurement) is the energy needed for the π-electron traveling from one macromolecule to another if orbitals with the same energy levels exist between the complex molecules[8,44,50] (see Fig. 6). The activation energies E_{intra} and E_{inter} were calculated from the slopes of the plots shown in Fig. 6(b), and the values are tabulated in Table 5. Obviously, the values of E_{intra} are higher than those of E_{inter} due to the restriction of the excited free carriers within the molecule by the barriers macromolecules. Noteworthy, the differences in the activation energies from complex to another may be due to contact resistance resulting from the different surface ratios of the four complexes.

The thermoelectric properties of the Ni(II) NCs were studied by measuring the Seebeck coefficient (S) as a function of temperature within a temperature range $83\,K \leq T \leq 313\,K$. Generally, the conduction mechanism of all NCs is governed by holes,[51–53] where the Seebeck coefficient has positive values over the whole range of temperatures. The Seebeck coefficient increases with the increase of temperature (Fig. 7). This behavior is typically a feature of degenerate semiconductor. Assuming that the material is a quasi-free electron system, the temperature dependence of the diffusion contribution

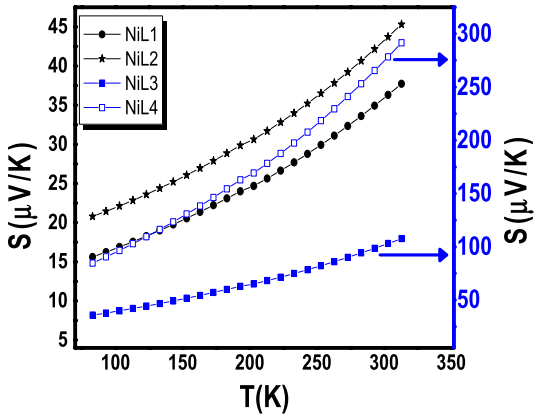

Fig. 7. Seebeck coefficient versus temperature of the Ni NCs and NiO NPs.

to thermopower in degenerate semiconductors is described by the following formula[54]:

$$S = \frac{\pi^2 k_B^2 T}{3eE_f}. \tag{2}$$

The E_f value is calculated for all samples and tabulated in Table 5. The room temperature Seebeck coefficient values S_{300} of NiL_1, NiL_2, NiL_3 and NiL_4 are $37\,\mu V/K$, $46.2\,\mu V/K$, $101.2\,\mu V/K$ and $292.6\,\mu V/K$, respectively. These values are much higher than those reported for other Schiff base complexes, indicating that the materials under study are promising for using as thermoelectric generators. For comparison, Li *et al.*[55] reported a value $S_{300} = 4.5\,\mu V/K$ for 2-(2-naphthalen-1-yl)vinyl)-thiophene Schiff base). Also, Gao and Chen[56] studied the effect of single wall carbon nanotubes (SWCNTs) content on the Seebeck coefficient value of poly-Schiff bases with 1,4-diaza-buta-1,3-diene structures. They recorded a value of $S_{300} \sim 55\,\mu V/K$ for the composite of 10% SWCNTs which decreases significantly with the increase of SWCNTs content to reach $\sim 43\,\mu V/K$ for the composite of 75% SWCNTs. The decrease of S was attributed to the giant conductivity of SWCNTs.

The magnetic properties of nanomaterials have been believed to be highly dependent on a lot of factors, for instance, the structure, size and shape of the grain, crystallinity, magnetization and applied field direction, lattice spacing, chemical composition, temperature, defect concentration, atomic order, impurities and so on. The DC magnetic measurements of the synthesized Ni(II) NCs were carried out by measuring the hysteresis (M–H) loops in Fig. 8. The data reveal that the materials have a small area

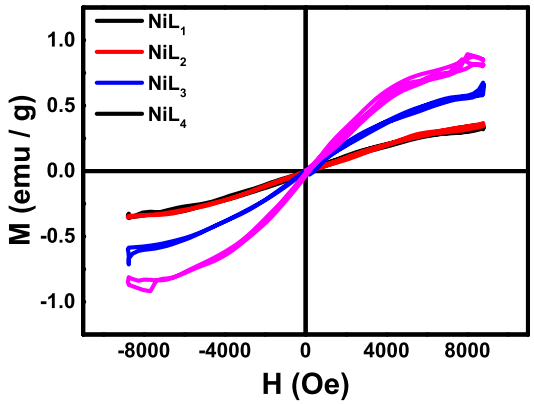

Fig. 8. Room temperature hysteresis loops of Ni(II) NCs.

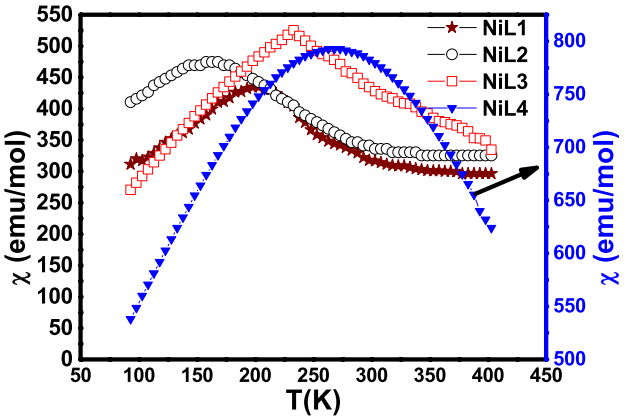

Fig. 9. AC susceptibility versus temperature curves of (a) Ni (II) NCs and (b) NiO NPs.

Table 6. The saturation magnetization M_s, coercivity H_c and T_N for all complexes and NiO nanoparticle.

	NiL_1	NiL_2	NiL_3	NiL_4
$M_{10,000\,Oe}$ (emu/g)	0.34	0.36	0.85	0.91
H_c (Oe)	98	76	31	53
T_N (K)	238	213	273	282

of hysteresis, which suggests the existence of a weak ferromagnetic ordering. The ferromagnetic behavior of the Ni(II) NCs is due to the Ni incorporation in the ligand matrix. Noteworthy, the $M \times H$ curves do not exhibit saturation up to an applied magnetic field 10,000 Oe indicating the nanometric size of the synthesized materials.[57,58] The saturation magnetization at 10,000 Oe $M_{10,000\,Oe}$ and coercivity H_c are both estimated for the materials under study and tabulated in Table 6. The variation of $M_{10,000\,Oe}$ values of the Ni(II) NCs is attributable to the variation of the exchange interaction between atoms at the surface of the particles in direct contact and dipole–dipole interactions in the samples.[43] In our case, the dipole–dipole interactions have the major effect due to the high magnetic moment per nanoparticle μ_p (calculated in the next section), which contributes to the magnetic properties even if the magnetic NPs were embedded or coated with non-magnetic material.[59,60] The changes in the coercivity (see Table 6) are mainly related to magnetocrystalline anisotropy since the increase/decrease in H_c means increase/decrease in the magnetic anisotropy.[60]

AC susceptibility measurements are crucial method to confirm spin cluster/glass behavior, complex spin states and phase transitions.[60] In this work, the AC susceptibility was measured as a function of temperature to study the dynamic behavior of magnetization in the samples. The measurements were carried out at a frequency of 0.3 kHz and magnetic field of 250 μT in a temperature range 90–405 K. In Fig. 9, χ versus temperature plot of each sample exhibits a peak at a certain temperature where it increases with the increase of temperature up to a certain value T_N and then decreases illustrating antiferromagnetic–paramagnetic transition. An estimate of the Néel temperature T_N was made from derivative of the χ–T plots and the values are depicted in Table 6. The difference of T_N values of the complexes can be attributed to a lot of factors that affect the antiferromagnetic interaction and Néel temperature, for instance, the coordination geometry of the compounds, oxidation state of metal cation (a greater charge pulls ligands more strongly toward the metal and therefore influences the splitting of the energy levels more) and size of the metal cation. Generally, the dynamic behavior in nanosized structure can be classified into two types. The first type originates from the broad distribution of the relaxation times and results from the anisotropy energy barriers. This type dominates in the non-interacting particles, in which the relaxation of the magnetic moments is affected mainly by the particle energy barrier that depends on the magnetic anisotropy which in turn depends on the particle size. The second dynamic behavior type becomes significantly effective in the dense magnetic NP systems in which frustration of magnetic moments occurs due to the dipolar interactions between the particles.[61,62] Dipolar interactions affect the magnetic properties significantly, particularly for the magnetic NPs with a high magnetic moment μ_p. On the other side, the magnetic

NPs of small μ_p have weak dipolar interactions, whereas the magnetic exchange interactions between atoms at the surface of the NPs in direct contact have a major effect on the magnetic properties. Magnetic moment μ_p values of the samples were determined at room temperature according to the following relation:

$$\mu_p = 2.83\sqrt{\chi_M T}, \tag{3}$$

where T is the temperature and χ_M is the molar magnetic susceptibility. The calculated magnetic moment values of Ni(II) NCs were found to be relatively weak (in the range 2.50–2.74 B.M.), indicating that the dipolar interaction minorly contributes to the dynamic magnetic behavior of the NCs.

4. Conclusions

This work presents a study on the electric, thermoelectric and magnetic properties of four nanosized Ni(II) imine complexes with general formulae ($[Ni(C_{12}H_{10}N_3O_4Br)]\cdot 2H_2O$, $[Ni(C_{16}H_{11}N_3O_4)]\cdot 2H_2O$, $[Ni(C_{21}H_{14}N_5O_8Br)]$ and $[Ni(C_{25}H_{17}N_5O_8)]\cdot 1/2H_2O$). The NCs show p-type degenerate semiconductor features. The electrical conduction in the NCs is governed by intermolecular and intramolecular carrier transfer mechanisms. The NCs show weak ferromagnetic phase at room temperature due to the incorporation of the Ni metal in the ligand matrix and the uncompensated magnetic moments on the surface, respectively. On the other side, the materials show antiferromagnetic–paramagnetic transition at certain temperatures.

References

1. M. Layek, M. Ghosh, S. Sain, M. Fleck, P. T. Muthiah, S. J. Jenniefer, J. Ribas and D. Bandyopadhyay, *J. Mol. Struct.* **1036**, 422 (2013).
2. L. H. Abdel-Rahman, A. M. Abu-Dief, R. M. El-Khatib and S. M. Abdel-Fatah, *J. Photochem. Photobiol. B* **162**, 298 (2016).
3. A. M. Abu-Dief and I. M. A. Mohamed, *J. Basic Appl. Sci.* **4**, 119 (2015).
4. L. H. Abdel-Rahman, A. M. Abu-Dief, M. S. S. Adam and S. K. Hamdan, *Catal. Lett.* **146**, 1373 (2016).
5. L. H. Abdel-Rahman, N. M. Ismail, M. Ismael, A. M. Abu-Dief and E. Abdel-Hameed Ahmed, *J. Mol. Struct.* **1134**, 851 (2017).
6. D. Baudouin, U. Rodemerck, F. Krumeich, A. de Mallmann, K. C. S. Zeto, H. Ménard, L. Veyre, J. P. Candy, P. B. Webb, C. Thieuleux and C. Copéret, *J. Catal.* **297**, 27 (2013).
7. R. K. Dani, M. K. Bharty, S. K. Kushawaha, Om Prakash, R. K. Singh and N. K. Singh, *Polyhedron* **65**, 31 (2013).
8. S. Sarkar, Y. Aydogdu, F. Dagdelen, B. B. Bhaumik and K. Dey, *Mater. Chem. Phys.* **88**, 357 (2004).
9. N. Bayal and P. Jeevanandam, *J. Nanopart. Res.* **15**, 2066 (2013).
10. M. Tadic, M. Panjan, D. Markovic, B. Stanojevic, D. Jovanovic, I. Milosevic and V. Spasojevic, *J. Alloys Compd.* **586**, 322 (2014).
11. S. Saravanakumar, R. Saravanan and S. Sasikumar, *Chem. Pap.* **68**, 788 (2014).
12. K. Karthik, G. K. Selvan, M. Kanagaraj, S. Arumugam and N. V. Jaya, *J. Alloys Compd.* **509**, 181 (2011).
13. B. J. Simmons, N. A. Weires, J. E. Dander and N. K. Garg, *ACS Catal.* **6**, 3176 (2016).
14. H. Xu, J. B. Diccianni, J. Katigbak, C. Hu, Y. Zhang and T. Diao, *J. Am. Chem. Soc.* **138**, 4779 (2016).
15. Y. Xiao, Y. Qin, M. Yi and Y. Zhu, *J. Clust. Sci.* **27**, 2013 (2016).
16. A. P. Mishra and R. K. Jain, *J. Chem. Pharm. Res.* **2**, 51 (2010).
17. A. M. Asiri and K. O. Badahdah, *Molecules* **12**, 1796 (2007).
18. E. M. M. Ibrahim, L. H. Abdel-Rahman, A. M. Abu-Dief, A. Elshafaie, S. K. Hamdan and A. M. Ahmed, *Mater. Res. Bull.* **99**, 103 (2018).
19. M. A. Neelakantan, M. Esakkiimmal, S. S. Mariappan, J. Dharmaraja and T. Jeyakumar, *Ind. J. Pharm. Sci.* **72**, 216 (2010).
20. A. A. M. Belal, I. M. El-Deen, N. Y. Farid, R. Zakaria and M. S. Refat, *J. Spectrochim. Acta A* **149**, 771 (2015).
21. A. K. S. Gupta and V. D. Barhate, *Res. J. Pharm. Biol. Chem. Sci.* **3**, 1013 (2012).
22. A. N. M. A. Alaghaz, M. E. Zayed, S. A. Alharbi and R. A. A. Ammar, *J. Mol. Struct.* **1087**, 60 (2015).
23. G. Grivani, M. Vakili, A. D. Khalaji, G. Bruno, H. A. Rudbari, M. Taghavi and V. Tahmasebi, *J. Mol. Struct.* **1072**, 77 (2014).
24. A. D. Khalaji, M. Nikookar and D. Das, *J. Therm. Anal. Calorim.* **115**, 409 (2014).
25. L. H. Abdel Rahman, A. M. Abu-Dief, N. A. Hashem and A. A. Seleem, *Int. J. Nano Chem.* **1**, 79 (2015).
26. L. H. Abdel-Rahman, A. M. Abu-Dief, R. M. El-Khatib and S. M. Abdel-Fatah, *Bioorg. Chem.* **69**, 140 (2016).
27. L. H. Abdel-Rahman, A. M. Abu-Dief, M. O. Aboelez and A. A. H. Abdel-Mawgoud, *J. Photochem. Photobiol. B: Biol.* **170**, 271 (2017).
28. L. H. Abdel-Rahman, R. M. El-Khatib, L. A. E. Nassr, A. M. Abu-Dief, M. Ismael and A. A. Seleem,

Spectrochim. Acta Part A: Mol. Biomol. Spectrosc. **117**, 366 (2014).
29. J. E. Kovacic, *J. Spectrochim. Acta Part A* **23**, 183 (1967).
30. E. Q. Castro, B. Bernes, A. T. Benavides, R. Contreras and H. Noth, *Polyhedron* **19**, 1479 (2000).
31. O. A. El-Gammal, G. A. El-Reash and S. F. Ahmed, *Spectrochim. Acta A* **135**, 227 (2015).
32. A. N. Alaghaz, M. A. Zayed and S. A. Alharbi, *J. Mol. Struct.* **1082**, 62 (2015).
33. L. H. Abdel-Rahman, A. M. Abu-Dief, R. M. El-Khatib 1, S. M. Abdel-Fatah and A. A. Seleem, *Int. J. Nano. Chem.* **2**, 83 (2016).
34. D. Ramakrishna, B. Bhat and R. R. Karvembu, *Catal. Commun.* **11**, 498 (2010).
35. W. Jamil, S. Solangi, A. M. Muhammed, K. Khan, K. M. Taha and M. M. Y. Khuhawar, *Arab. J. Chem.* doi:10.1016/j.arabjc.2015.02.015.
36. S. Brooker, S. S. Iremonger and P. G. Plieger, *Polyhedron* **22**, 665 (2003).
37. K. Naresh Kumar and R. Ramesh, *Polyhedron* **24**, 1885 (2005).
38. L. H. Abdel-Rahman, A. M. Abu-Dief, M. Ismael, M. A. A. Mohamed and N. A. Hashem, *J. Mol. Struct.* **1103**, 232 (2016).
39. Z. W. Zhao, K. Konstantinov, L. Yuan, H. K. Liu and S. X. Dou, *J. Nanosci. Nanotech.* **4**, 861 (2004).
40. Y. T. Li, C. W. Jan, Y. J. Zheng and D. Z. Liao, *Polyhedron* **17**, 1423 (1998).
41. M. Asadi, Z. Asadi, N. Savaripoor, M. Dusek, V. Eigner, M. R. Shorkaei and M. Sedaghat, *Spectrochim. Acta A* **136**, 625 (2015).
42. H. A. El-Asmy, I. S. Butler, Z. S. Mouhri, B. J. Jean-Claude, M. Emmam and S. I. Mostafa, *Inorg. Chim. Acta* **441**, 20 (2016).
43. M. A. Awad, A. M. Ahmed, V. O. Khavrus and E. M. M. Ibrahim, *Ceram. Int.* **41**, 10116 (2015).
44. M. G. Abd Elwahed, K. A. El Mankhly, A. Barakat and A. M. Amer, *Monatshefte Für Chemie* **127**, 1115 (1996).
45. L. H. Abdel Rahman, A. M. Abu-Dief, R. M. El-Khatib, S. M. Abdel-Fatah, A. M. Adam and E. M. M. Ibrahim, *Appl. Organometal. Chem.* **32**, e4174 (2018).
46. S. A. Ahmed, E. M. M. Ibrahim and S. A. Saleh, *Appl. Phys. A* **85**, 177 (2006).
47. M. M. Ibrahim, E. M. M. Ibrahim, S. A. Saleh and A. M. A. Hakeem, *J. Alloys Compd.* **429**, 19 (2007).
48. E. M. M. Ibrahim, A. M. Abu-Dief, A. Elshafaie and A. M. Ahmed, *Mater. Chem. Phys.* **192**, 41 (2017).
49. E. M. M. Ibrahim, L. H. Abdel-Rahman, A. M. Abu-Dief, A. Elshafaie and S. K. Hamdan, *Phys. Scrip.* **93**, 055801 (2018).
50. F. Gutmann, *Organic Semiconductors* (John Wiley Sons Inc., NewYork, London, Sydney, 1967).
51. M.-T. Chang, L.-J. Chou, C.-H. Hsieh, Y.-L. Chueh, Z. L. Wang, Y. Murakami and D. Shindo, *Adv. Mater.* **19**, 2290 (2007).
52. S. A. Saleh, S. A. Ahmed and E. M. M. Elsheikh, *J. Supercond. Novel Magnet.* **21**, 187 (2008).
53. S. A. Saleh, S. M. Khalil and E. M. M. Ibrahim, *Supercond. Sci. Technol.* **20**, 372 (2007).
54. H. Sato, T. Minami, S. Takata and T. Yamada, *Thin Solid Films* **236**, 27 (1993).
55. J. Li, C. Lai, X. Xiang and L. Wang, *Mater. Chem. C* **3**, 2693 (2015).
56. C. Gao and G. Chen, *J. Mater. Chem. A* **4**, 11299 (2016).
57. T. Jaumann, E. M. M. Ibrahim, S. Hampel, D. Maier, A. Leonhardt and B. Büchner, *Chem. Vapor Deposit.* **19**, 228 (2013).
58. E. M. M. Ibrahim, *J. Appl. Phys.* **113**, 154301 (2013).
59. P. M. Ponnusamy, S. Agilan, N. Muthukumarasamy, T. S. Senthil, G. Rajesh, M. R. Venkatraman and D. Velauthapillai, *Mater. Charact.* **114**, 166 (2016).
60. E. M. M. Ibrahim, S. Hampel, R. Kamsanipally, J. Thomas, K. Erdmann, S. Fuessel, C. Taeschner, V. O. Khavrus, T. Gemming, A. Leonhardt and B. Buechner, *Carbon* **63**, 358 (2013).
61. J. L. Dormann, D. Fiorani and D. Tronc, *J. Magn. Magn. Mater.* **202**, 251 (1999).
62. E. M. M. Ibrahim, S. Hampel, J. Thomas, D. Haase, A. U. B. Wolter, V. O. Khavrus, C. Täschner, A. Leonhardt and B. Büchner, *J. Nanopart. Res.* **14**, 1118 (2012).